MAST: An Earthquake-Triggered Landslides Extraction Method Combining Morphological Analysis Edge Recognition With Swin-Transformer Deep Learning Model

Yu Huang ⓘ, Jianqiang Zhang ⓘ, Haiqing He ⓘ, Yang Jia ⓘ, Rong Chen ⓘ, Yonggang Ge ⓘ, Zaiyang Ming ⓘ, Lili Zhang ⓘ, and Haoyu Li ⓘ

Abstract—Earthquake-triggered landslides (ETLs) are characterized by their extensive occurrences, having wide distributions. The conventional human–computer interaction extraction method is often time-consuming and labor-intensive, failing to meet the demands of disaster emergency response. There is a pressing need for a swift detection of ETLs. In this study, we introduce an ETLs extraction method (MAST) combining morphological analysis edge recognition with a Swin-Transformer (SWT) deep learning model, which is specifically designed for landslide extraction. The MAST model adopts a hierarchical construction approach akin to convolution neural networks, aiding in tasks such as target detection and semantic segmentation. To enhance the accuracy of landslide edge extraction, we incorporate an edge recognition algorithm based on the morphological analysis into the MAST model. This algorithm leverages morphological operations to extract the features of landslide boundaries. It effectively addresses issues such as discretization and irregularization of the extracted landslide boundaries, leading to more precise delineation of landslide boundaries. Drawing on UAV data collected from Wan Dong Village, De Tou Town, Sichuan Luding, China, during the 2022 Ms 6.8 Luding Earthquake, we conducted automated extraction of ETLs utilizing the MAST model. Experimental results demonstrate the superior performance of the MAST model compared to the traditional full convolution neural network (FCN) model and normal SWT model. The MAST model exhibits enhanced value in landslide extraction. Notably, it demonstrates a significant advantage in boundary extraction. Employing the Boundary IoU metric to evaluate the accuracy of ETLs extraction, the MAST model outperforms the SWT and FCN models at various distances.

Index Terms—Deep learning, earthquake-triggered landslides (ETLs), edge recognition, morphological analysis, transformer.

Yu Huang and Zaiyang Ming are with the Key Laboratory of Mountain Hazards and Earth Surface Process, Institute of Mountain Hazards and Environment, Chinese Academy of Sciences, Chengdu 610041, China, also with the Institute of Mountain Hazards and Environment, Chinese Academy of Sciences, Chengdu 610041, China, also with the Key Laboratory of Mine Environmental Monitoring and Improving Around Poyang Lake of Ministry of Natural Resources, East China University of Technology, Nanchang 330013, China, and also with the School of Surveying and Geoinformation Engineering, East China University of Technology, Nanchang 330013, China (e-mail: huangyu@ecut.edu.cn; Mingzy@ecut.edu.cn).

Jianqiang Zhang, Rong Chen, and Yonggang Ge are with the Key Laboratory of Mountain Hazards and Earth Surface Process, Institute of Mountain Hazards and Environment, Chinese Academy of Sciences, Chengdu 610041, China, and also with the Institute of Mountain Hazards and Environment, Chinese Academy of Sciences, Chengdu 610041, China (e-mail: zhangjq@imde.ac.cn; rongchen@imde.ac.cn; gyg@imde.ac.cn).

Haiqing He is with the Key Laboratory of Mine Environmental Monitoring and Improving Around Poyang Lake of Ministry of Natural Resources, East China University of Technology, Nanchang 330013, China, and also with the School of Surveying and Geoinformation Engineering, East China University of Technology, Nanchang 330013, China (e-mail: hehaiqing@ecut.edu.cn).

Yang Jia is with the Sichuan Highway Planning, Survey, Design and Research Institute, Ltd., Chengdu 610041, China (e-mail: jiayang@schdri.com).

Lili Zhang and Haoyu Li are with the Key Laboratory of Mountain Hazards and Earth Surface Process, Institute of Mountain Hazards and Environment, Chinese Academy of Sciences, Chengdu 610041, China, also with the Institute of Mountain Hazards and Environment, Chinese Academy of Sciences, Chengdu 610041, China, and also with the University of Chinese Academy of Sciences, Beijing 100049, China (e-mail: zhanglili@imde.ac.cn; lihaoyu231@mails.ucas.ac.cn).

Digital Object Identifier 10.1109/JSTARS.2023.3342989

I. INTRODUCTION

O N SEPTEMBER 5, 2022, a seismic event of magnitude 6.8 shook Luding County, situated in the Ganzi Tibetan Autonomous Prefecture within Sichuan Province. This seismic activity resulted in a considerable number of landslides, triggered by the ground shaking and surface rupture stemming from the earthquake. These earthquake-triggered landslides (ETLs) have effectively obstructed roads and rivers, engulfed towns, and villages, severely impeding postdisaster rescue operations. Consequently, they have exacerbated the direct damage caused by the earthquake and stand as one of the natural disasters responsible for severe human casualties and extensive property damage. Given these implications, the precise identification of ETLs emerges as an urgent and indispensable task in earthquake rescue and relief efforts [1], [2].

ETLs are typically analyzed through visual or automated methods. Visual extraction primarily relies on the expertise and experience of specialists in landslides, involving manual analysis of remote-sensing images to determine the location or boundaries of the landslides. Visual extraction takes into account the color tone, texture, development location, geometric shape, and other features of the landslide on the remote-sensing image, and the extraction results have high accuracy, but it is

time-consuming and laborious, and in addition, this method is affected by individual experts, which leads to differences in the results of the judgment. The automatic extraction method is to transform the experience of visual extraction into the methods and rules of remote-sensing software and utilize computers to automatically identify landslides. Compared with visual interpretation, automatic extraction is greatly affected by the quality of remote-sensing images, and the recognition accuracy is relatively low. In recent years, the development of machine learning methods has brought new opportunities in the automatic extraction of ETLs, such as support vector machine (SVM) and random forest. SVM is a supervised learning algorithm, and in automatic ETLs extraction, SVM can be trained with labeled landslide and nonlandslide samples to learn the boundary features and classification rules of landslides [3], [4], [5], [6]. SVM exhibits superior classification performance and generalization ability in the context of landslide boundary extraction. It excels at accurately delineating boundaries from new ETLs data. On the other hand, random forest employs an integrated learning approach by constructing multiple decision trees and amalgamating them for classification or regression tasks [7], [8]. In the automated extraction of ETLs, RF leverages the aggregated decisions from multiple decision trees to ascertain landslide boundaries. RF demonstrates robustness and resistance to overfitting, proficiently managing noise and uncertainty present in ETLs data [9], [10], [11], [12]. In addition to SVM and RF, various enhanced machine learning approaches have found application in automated ETLs extraction. For instance, neural-network-based methodologies, such as convolutional neural networks (CNNs) and recurrent neural networks (RNNs), can adeptly discern spatial and temporal features of landslides from seismic data, significantly enhancing the precision of landslide extraction [13], [14], [15], [16], [17], [18], [19], [20], [21], [22], [23], [24], [25], [26], [27], [28]. For instance, Ramdhoni et al. [14] employed the Smorph method to perform landslide extraction. This method involves utilizing slope and slope shape to construct a transformation matrix, achieving a landslide extraction accuracy of 79.54%[14]. Sameen and Pradhan [20] introduced a landslide detection method utilizing residual networks. This approach enhances network performance by fusing feature information within the same design, with the F1 score of 77% and mIoU of 77.20% [20]. Meanwhile, some cutting-edge research has combined multisource remote-sensing data for land cover classification. Li et al. [29], [30] proposed a spatial logic aggregation network with morphological transformation for tree species classification. Additionally, they introduced a Representation-enhanced Status Replay Network (RSRNet), which includes modal and semantic augmentation enhancement to enhance the transferability and discreteness of feature representation, reduces the impact of representation bias in the feature extractor, and alleviates the bias of the classifier while maintaining the stability of the decision boundary. The SRS was built to regulate the learning and optimization of the classifier. The RSRNet has demonstrated superiority in multisource remote-sensing image classification [29], [30].

In recent years, self-attention networks, such as the transformer, have emerged as a groundbreaking approach in natural language processing and image segmentation [31], [32].

For instance, Van Nguyen et al. [33] developed a lightweight transformer-based toolkit for multilingual natural language processing. This toolkit surpasses previous multilingual NLP pipelines in tasks, such as sentence segmentation and part-of-speech tagging [33]. Maria et al. [34] conducted an investigation into the viability of transformer-based solutions for medical image segmentation tasks. The study introduces the medical transformer, which undergoes evaluation using three distinct medical image segmentation datasets. The results demonstrate its superior performance [34]. The transformer architecture has shown remarkable advancements in image analysis tasks, such as image categorization and object detection. For instance, Zhao et al. [35] explored its potential in 3-D point cloud processing. They developed self-attentive networks for semantic scene segmentation, part-of-speech segmentation, and object categorization. The achieved mean Intersection over Union (mIoU) on region 5 of the S3DIS dataset, commonly utilized for large-scale semantic scene segmentation, reached 70.4%[35].

Various enhanced machine learning methods have demonstrated promising performance in the automated extraction of ETLs. However, several challenges persist. First, labeling ETLs data demands substantial time and expertise. Additionally, the morphology and features of landslides are influenced by multiple factors, including geological conditions, surface morphology, and seismic intensity, necessitating robust boundary extraction algorithms. Accurate identification of ETL edges enables early implementation of appropriate measures to mitigate potential risks. Nevertheless, traditional semantic segmentation detection methods such as average intersection and merger ratio, and F1 score often struggle to yield satisfactory results due to the complexity and noise interference in ETL images [36].

Therefore, in this study, we introduce an ETLs extraction method (MAST), which combines morphological analysis edge recognition with Swin-Transformer (SWT) deep learning model. It integrates a morphological edge detection algorithm for precise landslide extraction. The research focused on seismic landslides in the Wan Dong Village of Detuo Town, Luding County. The introduction of the Boundary IoU value as a novel evaluation metric for landslide boundary extraction precision allowed for a targeted, detailed, and quantitative comparison of the results obtained by the MAST, normal SWT, and traditional full convolution neural network (FCN) model. The study demonstrates the applicability of MAST in the field of ETLs extraction and its superiority in landslide boundary extraction. Moreover, it provides support for the enhanced applicability and effectiveness of deep learning methods in the domain of seismic landslide extraction.

II. Study Area and Datasets

On September 5, 2022, a magnitude 6.8 earthquake struck Luding County, Sichuan Province, China, at a depth of 16 km. The epicenter was pinpointed at 29.59°N latitude and 102.08°E longitude, triggering over 8000 earthquake-induced avalanches and landslides. For this research, the study area was designated as Wandong Village in Detou Town, Luding County, spanning from 102.05° to 102.26° east longitude and 29.33° to 29.70° north latitude, covering approximately 9.26 km^2. The area is located 9.43 km from the earthquake center, experiencing a seismic
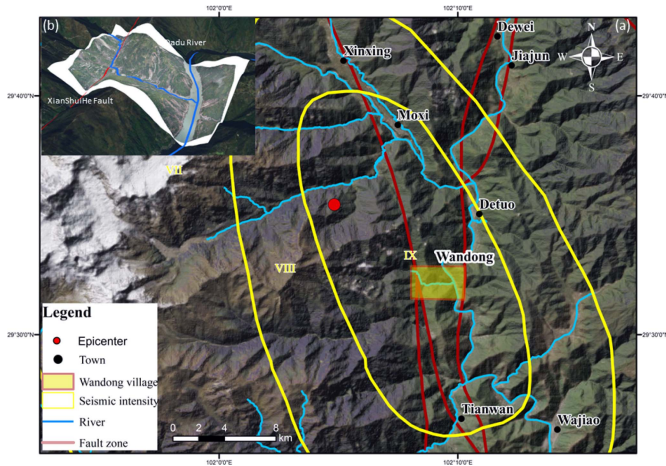
Fig. 1. (a) Location map of the study area. (b) Terrain schematic of the study area.

Fig. 2. Schematic diagram of MAST structure (SWT: This section illustrates the structure employed by Swin Transformer, where *Dn* represents the image being divided into blocks, and *Mn* represents the calculation of RGB channels. MA: This part pertains to the morphological analysis algorithm section, and different treatment methods are adopted for different ETLs).

intensity of magnitude 8. In the aftermath of the Luding earthquake, the Sichuan Geographic Information Bureau employed a UAV to capture aerial photographs of the earthquake-affected region on September 6, 2022. The UAV imagery was obtained at a spatial resolution of 0.2 m and underwent geometric corrections using ground control points. The Institute of Mountain Hazards and Environment, Chinese Academy of Sciences (CAS), utilized these images for ETL investigation using the visual extraction method. Concurrent field inspections were carried out to validate the findings. Ultimately, a total of 434 ETLs were identified in the study area, covering an area of 1.49 km^2 (Fig. 1). This catalog of ETLs serves as the reference data for automated identification in this study.

This study establishes a high-quality dataset of landslide samples to serve as the foundation for training the landslide recognition model. The UAV image is segmented into 512 × 512 pixel unit images, from which the landslide inventory map is generated. Data augmentation techniques are applied to enhance dataset diversity, mitigate overfitting, and bolster the model's generalization capability. The original landslide sample data are expanded by rotating, flipping, and mirroring the images, resulting in the acquisition of approximately 3000 images, constituting a set of highly precise landslide sample data. In the case of the landslide sample data, 70% is randomly chosen as the training set for model development while the remaining 30% is designated as the test set. All the experiments in this study are conducted with Python.

III. METHODS

In this research, we introduce the MAST approach, which integrates the SWT deep learning method with the morphological edge detection method. SWT, equipped with a hybrid loss function, serves as a feature extractor to capture crucial features in ETLs images. This extracted information is then combined with the morphological edge detection to improve the identification of ETL boundaries (see Fig. 2). MAST harnesses the outstanding performance of SWT in computer image recognition. Additionally, it addresses issues such as the discretization and irregularity of extracted landslide boundaries through
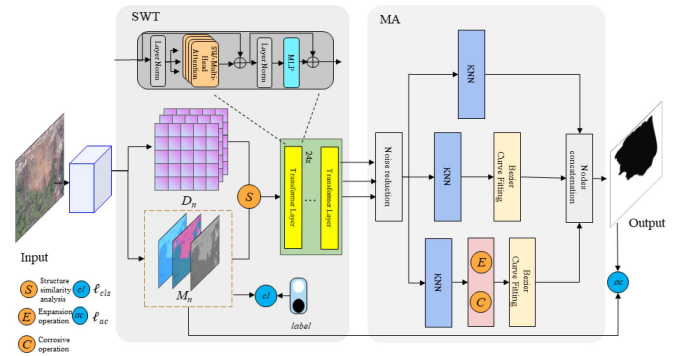
the morphological edge detection method, thereby enhancing accuracy in the automated extraction of ETLs.

A. Improved SWT With Hybrid Loss Function

SWT stands out as an advanced deep learning model for exceptional performance in computer vision. Its architecture resembles the hierarchical structure of convolutional networks, progressively halving the resolution and doubling the number of channels through successive layers. The model adopts a hierarchical design comprising four stages, each of which incorporates two components: 1) patch merging and 2) SWT [37], [38]. The patch merging process initiates at the beginning of each stage, involving downsampling. Its purpose is to lower resolution and fine-tune channel numbers, creating a hierarchical design. Notably, this approach, unlike traditional pooling, avoids information loss. The structure of the SWT block closely resembles that of the standard transformer block. However, a key distinction lies in its innovative hierarchical attention mechanism. This mechanism confines attention computation (multihead self-attention) to specific windows. By substituting the conventional multihead self-attention (MSA) with the moving window multihead self-attention (SW-MSA), the image gets broken down into mask blocks of varied scales. Subsequently, a moving window is employed to establish connections among these mask blocks. This alteration significantly enhances target detection and image classification performance. Consequently, the SWT showcases notable attributes including high scalability, adeptness in handling diverse image sizes, and outstanding parametric and computational efficiency. In this article, the number of transformer layers is set to 10, attention head count 8, the SW-MSA window size is set to 15 × 15, and the optimizer is selected as the Adam optimizer.

The calculation of the loss function l for the transformer model is

$$\iota = \lambda_{cls}\iota_{cls}. \tag{1}$$

The variable λ_{cls} represents the cross-entropy loss function, often utilized to gauge the disparity between two probability distributions, particularly in classification scenarios. It quantifies

the dissimilarity between the predicted probability distribution generated by the model and the actual label distribution. In the context of binary classification, the formulation of the cross-entropy loss function is as follows:

$$\iota_{cls} = -\frac{1}{n}\sum_{k}^{K}\left[y_k \log\left(\frac{1}{1+e^{-Z_k}}\right) \right.$$
$$\left. + (1-y_k)\log\left(\frac{e^{-Z_k}}{1+e^{-Z_k}}\right) \right]. \tag{2}$$

Given the challenges associated with vanishing gradients and the insufficient uncertainty captured by the cross-entropy loss function λ_{cls}, this study adopts a hybrid loss function, encompassing the cross-entropy loss function λ_{cls} and region contrast loss functions λ_{ac}, the combined loss function is computed as a weighted sum of these components using the following equation:

$$\iota = \lambda_{cls}\iota_{cls} + \lambda_{ac}\iota_{ac} \tag{3}$$

In the formula, $\lambda_{cls} = 0.7, \lambda_{ac} = 0.3$; ι_{ac} represents a region contrast loss function utilized to guide the original class activation mapping to emphasize absent objects in the image, offering supplementary constraints on the feature representation. This function is predominantly invoked in this article to address the issue of vanishing gradients associated with the cross-entropy loss function, which is calculated as

$$\iota_{ac} = \frac{1}{n}\sum_{k}^{K} \mathrm{SL}_1\left(M_k, \hat{M}_k\right) \tag{4}$$

$$\mathrm{SL}_1(y,\hat{y}) = \begin{cases} 0.5(\hat{y}-y)^2, |\hat{y}-y| < 1 \\ |\hat{y}-y| - 0.5, |\hat{y}-y| \geq 1 \end{cases}. \tag{5}$$

SL_1 stands for smooth L1 loss function.

The enhancement of the loss function in this article enables the model to optimize its performance in the landslide extraction task. It effectively addresses the issue of gradient vanishing, consequently reducing overfitting to local details in the training data. This refinement facilitates a more accurate capture of the data's overall structure and key features.

B. Landslide Edge Detection Using Morphological Analysis

Conventional machine extraction methods operate at the pixel level and interpret slope edges as jagged boundaries in many cases, which do not align with reality; the results often contain numerous fragmented polygons, requiring time and effort to manually integrate and rectify. In this study, we utilize morphological analysis and SWT-result-based edge detection to rectify the fragmented, jagged, and irregularly defined landslide boundaries [39], [40], [41].

The steps for landslide edge detection based on the morphological analysis are as follows.
1) In image preprocessing, we utilize sample quantization or coding to transform the initial continuous space and luminance into discrete representations. To enhance computational and output efficiency, the raw image is partitioned

into an $M \times N$ array with a fixed unit size

$$F_M(x,y) = \begin{Bmatrix} F(0,0) & \dots & F(0, N-1) \\ \vdots & \ddots & \vdots \\ F(M-1, 0) & \dots & F(M-1, N-1) \end{Bmatrix}. \tag{6}$$

Preprocessing of landslide images involves noise reduction and enhancement of edge information. During this step, voids within the landslide are filled, and any debris or deformations resulting from the interpretation are removed. The UAV image resolution in this study is 0.2 m. To reduce noise and facilitate the subsequent extraction of landslide edge structures, we uniformly remove debris polygons at the pixel level in a 5×5 pattern.
2) *Defining Structural Elements:* Given that the landslide comprises irregular polygons of various sizes, this study addresses the attribution of deciphering result fragments in small areas. This study employs the nearest neighbor algorithm, attributing deciphering result fragments of small areas to the landslide body with the nearest Euclidean distance. Concurrently, the connecting area between them is replenished

$$F_L = KNN(F_l, F_L) \tag{7}$$

where F_l represent deciphering result fragments in small areas; F_L represent the landslide structural elements; KNN represent the nearest neighbor algorithm.
3) *Expansion Operation:* Conducts an image expansion operation using the updated defined structural elements. This operation expands the brightly lit regions, enhancing the edge features of the landslide. This process widens the region at the landslide's boundary, filling cavities, and narrow gaps in the foreground, enhancing edge continuity

$$F_L \oplus D = F_L|(D)_F \bigcap F_L \neq \oslash \tag{8}$$

where F_L represent the landslide structural elements; D represent the area which to extend.
4) *Corrosive Operation:* Applying an erosion operation to the image using structural elements. This operation decreases high-brightness areas, resulting in more compact boundary features for the landslide

$$F_L \ominus D = F_L|(D)_F \in F_L \tag{9}$$

where F_L represent the landslide structural elements; D represent the area which to corrode.
5) *Fitting Extraction:* The morphology of landslide edges is complex and influenced by various factors, and different types of landslides may show different morphologies. However, it is difficult for the edges of landslides to show multiple consecutive turns or high curvature changes. In this article, by calculating the difference between the expansion operation and the erosion operation, we can approximate the location of the landslide boundary and extract its structural elements.
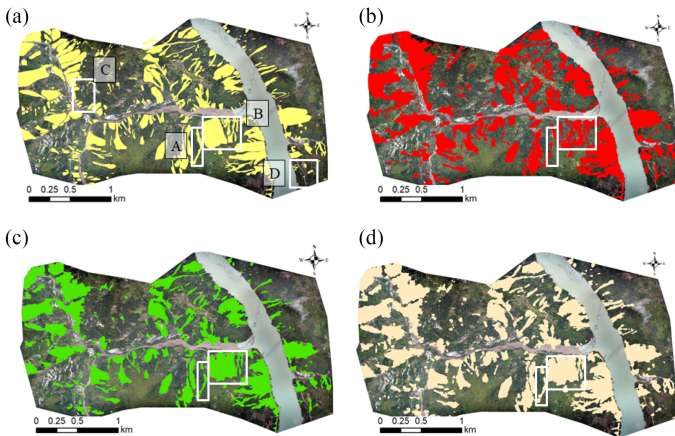
Fig. 3. (a) Visually interpreted landslide area. (b) FCN extracted landslide area. (c) SWT extracted landslide area. (d) MAST extracted landslide area.

6) *Boundary Optimization:* Employ smoothing algorithms and other edge optimization methods to eliminate unnecessary noise and details, enhancing the clarity and continuity of the landslide boundary. This process aims to optimize the boundary and improve accuracy.

IV. RESULTS

A. Remote-Sensing Extraction Results for ETLs

Landslides were extracted from UAV images using the MAST model [see Fig. 3(b)]. These extractions were then compared and analyzed in comparison to those obtained through the SWT model [see Fig. 3(c)] and the deep fully CNN model [see Fig. 3(d)] [38]. Specifically, FCN extracted landslides covering an area of 1.43 km^2, SWT extracted landslides covering 1.46 km^2, and MAST extracted landslides covering 1.46 km^2. This analysis indicates that landslides extracted using the SWT and MAST models more closely align with the reference ETLs catalog. The comparison of landslide area and distribution reveals notable differences. The FCN model tends to fragment large landslides (e.g., landslide A), forming multiple smaller ones, whereas the SWT and MAST models better capture the entire landslide. Similarly, for extensive landslides (e.g., landslide B), the FCN model often misconstrues them as several smaller landslides while the SWT and MAST models accurately identify the complete landslide. However, in cases where landslides are interconnected, distinguishing and decomposing them proves challenging for all three methods. For instance, landslide C, situated on the right bank of a river, is identified by all three models as a single landslide, conflating it with a landslide on the left bank of the river. The MAST model displays an advantage in certain cases, such as landslide D, where the FCN and SWT models misidentify it while the MAST model closely aligns with the parameter data for the identified landslides.

B. Semantic Segmentation Accuracy

According to the results obtained from different models for ETL extraction, we constructed a confusion matrix for ETLs and no ETLs (refer to Table I). In the matrix, "P" denotes the positive region, signifying the area where ETLs are present, and "N" indicates the negative region, representing the area without ETLs. "TP" refers to the true-positive region, where ETLs are accurately identified, aligning with both actual and predicted positive conditions. On the other hand, "TN" signifies the true-negative region, correctly capturing the absence of landslides in both actual and predicted negative conditions. "FN" stands for the false-negative region, denoting areas misclassified as nonlandslides despite being actual landslides. Finally, "FP" refers to the false-positive region, representing areas incorrectly identified as landslides when they are not. Analyzing the confusion matrix results in Table I, we observe that FCN accurately extracted landslides covering an area of 1.23 km^2. In comparison, SWT and MAST demonstrated improved performance by identifying landslides covering 1.27 km^2 and 1.28 km^2, respectively. These values were 0.03 km^2 and 0.04 km^2 higher than FCNs extraction results. Notably, FCN failed to extract landslides covering 0.26 km^2, the highest among the three methods. In contrast, MAST achieved the best results with only 0.21 km^2 of extracted landslides.

Based on the confusion matrix, five metrics (see Table II) were calculated to obtain the overall accuracy, positive precision, recall, F1 score, and mean intersection and merger ratio (mIoU) to quantitatively compare the accuracy of different models for ETLs extraction.

Accuracy is the proportion of correct predictions to the total number of results and is given as

$$\text{Accuracy} = (\text{TP} + \text{TN})/(\text{TP} + \text{TN} + \text{FP} + \text{FN}). \quad (10)$$

TABLE I
CONFUSION MATRIX FOR LANDSLIDE EXTRACTION RESULTS

		Landslides(extracted) / km^2		Non-Landslides(extracted) / km^2	
Landslides	FCN	TP	1.23	FN	0.26
(1.49 km^2)	SWT		1.27		0.23
	MAST		1.28		0.21
Non-Landslides	FCN	FP	0.20	TN	7.57
(7.77 km^2)	SWT		0.19		7.57
	MAST		0.18		7.59

TABLE II
LANDSLIDE EXTRACTION AREA RESULTS FROM REMOTE-SENSING IMAGE

	FCN	SWT	MAST
Total area extracted /m^2	1425870	1461839	1464020
Accuracy	94.45%	95.51%	95.68%
False positive	2.91%	2.00%	1.94%
True positive	2.16%	2.54%	2.24%
Precision	86.01%	87.31%	88.93%
Recall	82.00%	84.73%	86.39%
F1 score	83.96%	86.01%	87.64%
mIoU	83.25%	84.99%	86.10%

Positive precision (precision) is the proportion of positive correct areas to the total positive data and is given by the formula

$$\text{Precision} = \text{TP}/(\text{TP} + \text{FP}). \qquad (11)$$

The recall rate (recall) reflects the ratio of ETLs samples predicted as correct to all actual ETLs samples and is given by the formula

$$\text{Recall} = \text{TP}/(\text{TP} + \text{FN}). \qquad (12)$$

The F1 index (F1-score) is the harmonic mean of precision and recall and is given by the formula

$$F1 = 2(\text{precision} \times \text{recall})/(\text{precision} + \text{recall}). \qquad (13)$$

The mean intersection and merger ratio (mIoU) is the average of the ratio of the intersection and merger sets of the 2 sets of true and predicted values and is given as

$$\text{mIoU} = (\text{TP}/(\text{TP} + \text{FP} + \text{FN}) + \text{TN}/(\text{TN} + \text{FP} + \text{FN}))/2. \qquad (14)$$

The eight metrics presented in Table II are highly representative within the chosen domain of image semantic segmentation. It is evident that both the MAST and SWT algorithms consistently outperform the FCN algorithm across most metrics. In terms of overall accuracy, both SWT and MAST surpass FCN by over 1%, with MAST exhibiting a slight advantage over SWT by 0.17%. Positive accuracy is notably higher with SWT at 1.3% over FCN; however, MAST further improves by 1.6% compared to SWT, showcasing its superior accuracy in ETLs extraction. This trend is similarly reflected in the mIoU values, where MAST exceeds FCN by 2.85% and surpasses SWT by 1.11%. In summary, the MAST algorithm consistently achieves superior accuracy in the task of landslide extraction. Nevertheless, it is essential to acknowledge that due to the relatively small landslide area in comparison to the nonlandslide area, traditional accuracy evaluation metrics may not effectively represent the disparities in ETLs extraction accuracy across various machine learning models.

V. DISCUSSION

A. Impact of Morphological Analysis on Landslide Boundary Extraction

In this study, we present a detailed comparison of landslide extraction boundaries using FCN, SWT, and MAST on UAV imagery (see Fig. 4). The MAST model, incorporating a morphological analysis step, demonstrates significant advantages in identifying landslide areas on an individual landslide level. Its extraction results align more closely with the objective characteristics of ETLs boundaries. By synthesizing deep learning models and morphological analysis, MAST effectively addresses morphological features inherent to landslides. It compensates for the limitations of deep learning models in handling complex features' boundaries, overcoming issues, such as debris polygons, incomplete landslide interpretation, hollow areas, and rugged landslide boundaries. Consequently, the boundary of the landslide is smoothed, eliminating the jagged state. This underscores MASTs performance in landslide extraction and analysis,
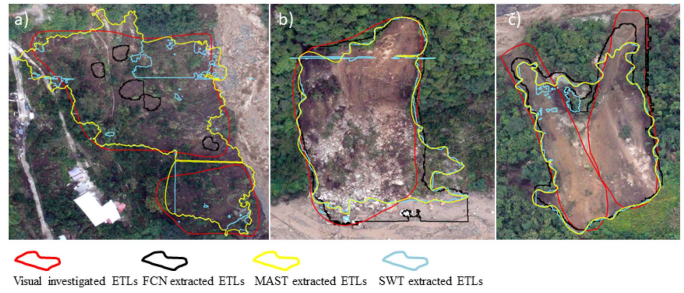

Fig. 4. Schematic diagram illustrating the extraction results of each method for a single landslide. (a) SWT landslide extraction result: contains numerous debris polygons. (b) SWT landslide extraction result: interprets a single landslide section as two separate landslide regions. (c) SWT extraction result: shows hollow areas within the landslide.

showcasing its prowess in integrating diverse technological tools to enhance model performance.

First, the MAST method effectively eliminates debris polygons. Both the SWT and FCN models tend to generate numerous debris polygons within landslide areas due to surface complexity and image coverage. This issue is nearly unavoidable following a landslide event. However, the introduction of morphological analysis in the MAST model allows for the removal of these debris polygons, thus rectifying the oversegmentation of individual landslides [see Fig. 4(a)]. In our study, FCN resulted in 37 609 debris polygons and SWT in 4978 debris polygons while the MAST model yielded none. Automated removal of debris polygons significantly reduces the time and labor required for manual clean-up.

Second, the MAST method addresses the challenge of a single landslide being extracted as multiple smaller landslides. This often arises due to the decomposition of ETLs into various stacking zones, with vegetation cover further complicating the situation. The SWT model, in particular, tends to classify these zones as distinct small landslides, a limitation not fully resolved by deep learning algorithms alone. The MAST model effectively separates these smaller landslides, reaggregates them into their primary landslide form [see Fig. 4(b)], and fills in the intervening connectivity, rectifying the problem of mistaking a single landslide for multiple smaller ones.

The third crucial improvement involves resolving hollow areas within landslide bodies. In some larger ETLs, fragmentation leaves parts of the vegetation intact within the landslide body, often unconnected to surrounding vegetation. Both the SWT and FCN models tend to misinterpret these vegetated areas within the landslide body as nonlandslide areas, resulting in hollow boundaries [see Fig. 4(c)]. To enhance extraction accuracy, the MAST model employs morphological analysis to fill these hollow regions. Utilizing area operations, it identifies independent areas within the polylines, examines their topology, and identifies overlapping regions. Since the ETLs considered occurred within a relatively recent timeframe, without overlapping old and new landslides, these identified overlapping regions are reassigned as parts of the landslides, effectively addressing the issue of hollow areas within the landslides.
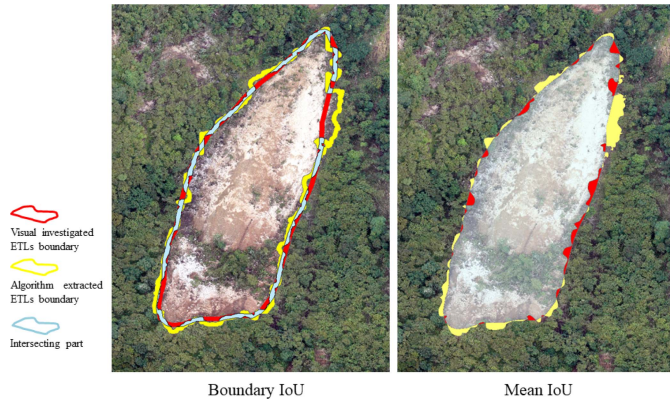
Fig. 5.   Schematic diagram of Boundary IoU and mIoU calculation methods.

B. Boundary Segmentation Calculation Metrics—Boundary IoU

The traditional parameters for evaluating the accuracy of automatic landslide extraction are predominantly influenced by the landslide area in relation to the nonlandslide area. Given that the landslide area is typically much smaller compared to the nonlandslide area, even a correct extraction of landslide areas with a low accuracy would result in a large correctly extracted nonlandslide area, inflating the overall accuracy. Furthermore, these evaluation metrics emphasize overall variability and may not effectively account for boundary consistency. In the domain of computer vision, deep learning has attained a high level of proficiency in landslide extraction applications. However, the differences in ETLs extraction among various deep learning models are marginal, rendering traditional accuracy evaluation parameters inadequate for characterizing extraction accuracy differences. To better elucidate these disparities in ETLs extraction achieved by distinct deep learning methodologies, this study employs Boundary IoU (see Fig. 5), a computational metric for boundary segmentation, to evaluate landslide extraction accuracy [42].

Boundary IoU represents an extension of IoU-based metrics, specifically designed for pixel-level boundary segmentation tasks aimed at accurately delineating object boundaries. Consequently, this parameter stands as a highly effective measure of the consistency between automatically extracted boundaries of ETLs and their true boundaries. Within the domain of image segmentation, the quality of boundary segmentation serves as a crucial reference index for determining the effectiveness of an algorithm. Currently prevalent mIoU-based AP metrics often lack sensitivity toward the segmentation quality of mask boundaries, contributing to the limited enhancement of mask boundary segmentation quality despite ongoing algorithmic optimizations in recent years. In contrast, Boundary IoU demonstrates sensitivity to the segmentation quality of object boundaries, providing a robust assessment of different segmentation algorithms concerning object boundaries.

Boundary IoU is calculated as

$$\text{Boundary IoU} = \frac{|(G_d) \cap G) \cap (P_d) \cap P)|}{|(G_d) \cap G) \cup (P_d) \cap P)|} \qquad (15)$$

TABLE III
BOUNDARY IoU CALCULATION INDICATORS

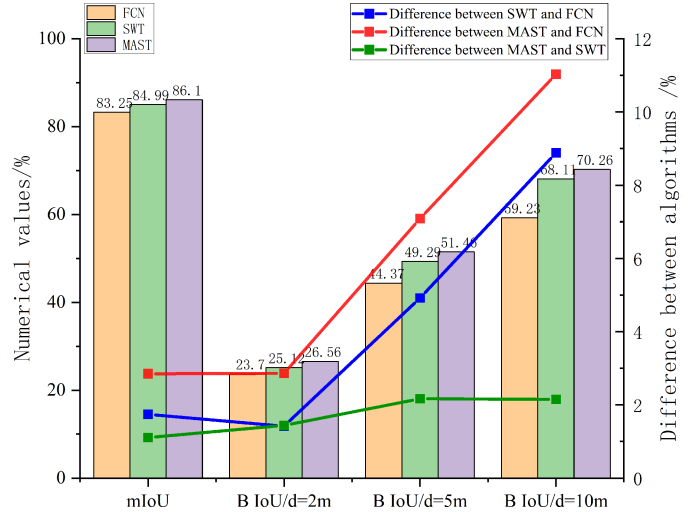| Notation	Definition
G	Ground truth binary mask
P	Prediction binary mask
G_1, P_1	Set of pixels on the contour line of the binary mask
G_d, P_d	Set of pixels on the boundary region of the binary mask
d	Width of the boundary region

Fig. 6.   Variances in values calculated by FCN, SWT, and MAST across various metrics are examined.

where G_d denotes the set of pixels whose distance from the contour of the ground truth mask is not greater than d, and P_d denotes the set of pixels whose distance from the contour of the predicted mask is not greater than d (see Table III).

The distance d controls the sensitivity of Boundary IoU. When d is sufficiently large, Boundary IoU is equivalent to Mask IoU. On the other hand, when d is relatively small, Boundary IoU disregards pixels in the mask that are distant from the boundary, placing more emphasis on segmentation quality near the object's boundary, even for larger-sized objects. The range of Boundary IoU values is from 0 to 1. A value closer to 1 indicates a higher overlap between the predicted boundary and the real boundary, signifying a more accurate prediction. The goal of the boundary segmentation algorithm is to strive for a Boundary IoU as close to 1 as possible to achieve precise boundary segmentation.

The calculation of Boundary IoU values for ETLs extracted by FCN, SWT, and MAST methods (see Fig. 6) demonstrates that MAST exhibits superior performance for d values of 2 m, 5 m, and 10 m, followed by SWT. The Boundary IoU values vary with different d values and display a discernible pattern. As the d value increases, the differences in Boundary IoU values of landslides extracted by different methods become more prominent, offering a clearer demonstration of the extraction boundary differences. For instance, at a d value of 2 m, the Boundary IoU values for the three methods are 23.7%, 25.12%, and 26.56%, respectively. The differences among the three methods are relatively small, with SWTs Boundary IoU being 1.42% higher than that of FCN,

and MASTs being 1.44% higher than SWTs. At a d value of 5 m, the Boundary IoU values for the three methods rise to 44.37%, 49.29%, and 51.46%, respectively. The differences between the three methods also escalate, with SWTs Boundary IoU being 4.92% higher than FCNs, and MASTs being 2.17% higher than SWTs. At a d value of 10 m, the Boundary IoU values for the three methods increase to 59.23%, 68.11%, and 70.26%, respectively. The differences between the three also intensify, with SWTs Boundary IoU being 8.88% higher than FCNs, and MASTs being 2.15% higher than SWTs. These fluctuations in Boundary IoU values for different methods illustrate that compared to the FCN model, the SWT model significantly improves accuracy in ETLs extraction. Moreover, MAST also enhances the accuracy of ETLs extraction, although the degree of improvement is relatively moderate. Simultaneously, this study aims to demonstrate the stability of the MAST model by calculating the variance of the boundary IoU results. At d values of 2 m, 5 m, and 10 m, the variances are 0.68, 0.39, and 0.34, respectively. These results indicate that MAST can maintain a relatively stable performance across different ETL scenarios.

In comparison to the traditional semantic segmentation index mIoU, FCN, SWT, and MAST all achieved scores higher than 83% (see Fig. 6). However, because the mIoU algorithm places greater emphasis on overall region identification, the differences in mIoU scores between different algorithms are relatively minor, making it less effective in reflecting MASTs enhancement in the landslide boundary extraction segment.

The disparity between MAST and SWT becomes more noticeable at mIoU and BIoU for d values of 2 m and 5 m. Specifically, at a d value of 5 m, SWT exhibits a 4.92% higher BIoU than FCN, and MAST surpasses SWT by 2.17% in BIoU. The BIoU difference is nearly twice that of mIoU. At a d value of 10 m, SWT achieves an 8.88% higher BIoU than FCN, with MAST exceeding SWT by 2.15% in BIoU. Here again, the difference in BIoU is considerably more pronounced than in mIoU. Notably, the BIoU difference between MAST and SWT stabilizes at approximately 2.17% for a d value of 5 m and 2.15% for a d value of 10 m, indicating a leveling off. Consequently, this study posits that the influence of morphological analysis on the specific boundary range between MAST and SWT remains within 10 m. This conclusion is substantiated by the fact that a range exceeding 10 m is sufficiently broad for seismic landslides, adequately covering the landslide range. The results of numerical BIoU calculations no longer yield significant differences. For d values of 5 m and 10 m, MAST outperforms SWT by 2.17% and 2.15%, respectively. Hence, beyond a distance value of 5 m, the integration of morphological analysis yields approximately a 2% improvement for MAST. However, due to the constraint imposed by the area of earthquake-induced landslides, the d value cannot be boundlessly increased.

VI. Conclusion

In this study, we enhance the SWT model by modifying its hybrid loss function and integrating a morphological edge detection method with morphological analysis, resulting in the MAST ETLs extraction model. We also introduce the Boundary

IoU method to evaluate ETLs extraction accuracy and draw the following conclusions from the comparison experiments.

1) The MAST model excels in landslide extraction. Compared to the traditional FCN model, MAST exhibits superior feature extraction and context understanding capabilities when processing landslide images. Its self-attention mechanism and hierarchical structure enable the capture of both detailed and global landslide information, thereby enhancing edge extraction accuracy at the semantic segmentation level. Overall, MAST achieves a 1.23% higher accuracy than FCN and a 0.17% higher accuracy than SWT. Positive accuracy is 2.92% higher than FCN and 1.62% higher than SWT. The mIoU is 2.85% higher than FCN and 1.11% higher than SWT. The morphological edge detection integrated into MAST significantly contributes to landslide boundary extraction. Through morphological operations such as swelling and erosion, it enhances the continuity and accuracy of landslide boundaries. This method effectively reduces noise and unnecessary details, especially in the treatment of debris polygons and segmented small broken landslides, thus improving edge detection accuracy and stability while preserving the shape and structural characteristics of the landslide boundary.

2) The introduced Boundary IoU in the experimental results showcases that more accurate landslide extraction results are achievable using the MAST method. According to the B IoU results, MAST performs better at d values of 2 m, 5 m, and 10 m. At a d value of 2 m, MASTs B IoU is 1.42% higher than FCN and 1.44% higher than SWT. At a d value of 5 m, MASTs B IoU surpasses FCN by 4.92%, and SWT by 2.17%. At a d value of 10 m, MASTs B IoU exceeds FCNs by 8.88%, and SWTs by 2.15%. This substantiates that MAST and SWT outperform the FCN model not only in traditional semantic segmentation but also in critical edge recognition. It highlights MASTs superior ability to recognize boundaries accurately and segment object edges precisely. Additionally, the introduction of morphological analysis has a limited effect on the specific boundary range of both MAST and SWT, staying within 10 m.

This study verifies the outstanding performance of the SWT model in the realm of ETLs machine learning. Moreover, the MAST model, an extension of the SWT model, enhances ETLs extraction accuracy further. Future efforts should concentrate on strengthening multisource data fusion, integrating various remote sensing, geographic information, and seismic monitoring data to enhance comprehensiveness and accuracy of extraction. Also, since the model used in this article is a UAV image, the data source is single and is affected by the nature of the UAV itself, which is subject to weather conditions. In addition, the ETLs extraction model needs to be enhanced with its generalization capability to incorporate multisource data in order to have wider applicability in landslide extraction in different regions, under different incentive conditions and with different geological scenarios. Integrating the results of the study with disaster emergency response and decision support systems is essential to provide timely and accurate information for disaster management and to minimize disaster losses.

REFERENCES

[1] J. Zhang et al., "Distribution patterns of landslides triggered by the 2022 Ms 6.8 Luding earthquake, Sichuan, China," *J. Mountain Sci.*, vol. 20, no. 3, pp. 607–623, Mar. 2023. [Online]. Available: https://link.springer.com/10.1007/s11629-022-7772-0

[2] Z. Xiao et al., "Analysis of spatial distribution of landslides triggered by the Ms 6.8 Luding earthquake in China on Sep. 5, 2022," *Geoenvironmental Disasters*, vol. 10, no. 1, pp. 1–15, Feb. 2023. [Online]. Available: https://geoenvironmental-disasters.springeropen.com/articles/10.1186/s40677-023-00233-w

[3] D. Costanzo, E. Rotigliano, C. Irigaray, J. D. Jiménez-Perálvarez, and J. Chacón, "Factors selection in landslide susceptibility modelling on large scale following the GIS matrix method: Application to the River Beiro Basin (Spain)," *Natural Hazards Earth Syst. Sci.*, vol. 12, no. 2, pp. 327–340, Feb. 2012. [Online]. Available: https://nhess.copernicus.org/articles/12/327/2012/

[4] G. Rajmohan, C. V. Chinnappan, A. D. J. William, S. C. Balakrishnan, B. A. Muthu, and G. Manogaran, "Revamping land coverage analysis using aerial satellite image mapping," *Trans. Emerg. Telecommun. Technol.*, vol. 32, no. 7, Jul. 2021, Art. no. e3927. [Online]. Available: https://onlinelibrary.wiley.com/doi/10.1002/ett.3927

[5] T. Kavzoglu, I. Colkesen, and E. Şahin, "Machine learning techniques in landslide susceptibility mapping: A survey and a case study," in *Landslides: Theory, Practice and Modelling*. Cham, Switzerland: Springer, 2018. [Online]. Available: https://www.semanticscholar.org/paper/f2f4a4cc8c7179f7a91d5b0c25a6ab8d5a79bc57

[6] M. Marjanović, M. Kovačević, B. Bajat, S. Mihalić, and B. Abolmasov, "Landslide assessment of the Starča Basin (Croatia) using machine learning algorithms," *Acta Geotechnica Slovenica*, vol. 8, pp. 45–55, 2011.

[7] S. J. Rigatti, "Random forest," *J. Insurance Med.*, vol. 47, no. 1, pp. 31–39, Jan. 2017. [Online]. Available: https://meridian.allenpress.com/jim/article/47/1/31/131479/Random-Forest

[8] J. L. Speiser, M. E. Miller, J. Tooze, and E. Ip, "A comparison of random forest variable selection methods for classification prediction modeling," *Expert Syst. Appl.*, vol. 134, pp. 93–101, Nov. 2019. [Online]. Available: https://linkinghub.elsevier.com/retrieve/pii/S0957417419303574

[9] B. T. Pham, D. T. Bui, I. Prakash, and M. B. Dholakia, "Rotation forest fuzzy rule-based classifier ensemble for spatial prediction of landslides using GIS," *Natural Hazards*, vol. 83, no. 1, pp. 97–127, Aug. 2016. [Online]. Available: http://link.springer.com/10.1007/s11069-016-2304-2

[10] M. Belgiu and L. Drăguţ, "Random forest in remote sensing: A review of applications and future directions," *ISPRS J. Photogrammetry Remote Sens.*, vol. 114, pp. 24–31, Apr. 2016. [Online]. Available: https://linkinghub.elsevier.com/retrieve/pii/S0924271616000265

[11] D. Seo, Y. Kim, Y. Eo, and W. Park, "Learning-based colorization of grayscale aerial images using random forest regression," *Appl. Sci.*, vol. 8, no. 8, Jul. 2018, Art. no. 1269. [Online]. Available: http://www.mdpi.com/2076-3417/8/8/1269

[12] W. Chen, Z. Sun, and J. Han, "Landslide susceptibility modeling using integrated ensemble weights of evidence with logistic regression and random forest models," *Appl. Sci.*, vol. 9, no. 1, Jan. 2019, Art. no. 171. [Online]. Available: https://www.mdpi.com/2076-3417/9/1/171

[13] C. Pelletier, G. Webb, and F. Petitjean, "Temporal convolutional neural network for the classification of satellite image time series," *Remote Sens.*, vol. 11, no. 5, Mar. 2019, Art. no. 523. [Online]. Available: https://www.mdpi.com/2072-4292/11/5/523

[14] F. Ramdhoni, A. Damayanti, and T. L. Indra, "Smorph application for landslide identification in Kebumen Regency," *IOP Conf. Ser.: Earth Environ. Sci.*, vol. 451, no. 1, Mar. 2020, Art. no. 012013. [Online]. Available: https://iopscience.iop.org/article/10.1088/1755-1315/451/1/012013

[15] Y. Wang, X. Wang, and J. Jian, "Remote sensing landslide recognition based on convolutional neural network," *Math. Problems Eng.*, vol. 2019, pp. 1–12, Sep. 2019. [Online]. Available: https://www.hindawi.com/journals/mpe/2019/8389368/

[16] C. Tang, J. Tang, C. J. van Westen, J. Han, O. Mavrouli, and C. Tang, "Modeling landslide failure surfaces by polynomial surface fitting," *Geomorphology*, vol. 368, Nov. 2020, Art. no. 107358. [Online]. Available: https://linkinghub.elsevier.com/retrieve/pii/S0169555X20303317

[17] H. Lu et al., "Landslides information extraction using object-oriented image analysis paradigm based on deep learning and transfer learning," *Remote Sens.*, vol. 12, no. 5, Feb. 2020, Art. no. 752. [Online]. Available: https://www.mdpi.com/2072-4292/12/5/752

[18] D. Cha, "Landslides detection and volume estimation in Jinbu area of Korea," *Forest Sci. Technol.*, vol. 14, pp. 61–65, 2018.

[19] W. Xia, J. Chen, J. Liu, C. Ma, and W. Liu, "Landslide extraction from high-resolution remote sensing imagery using fully convolutional spectral–topographic fusion network," *Remote Sens.*, vol. 13, no. 24, Dec. 2021, Art. no. 5116. [Online]. Available: https://www.mdpi.com/2072-4292/13/24/5116

[20] M. I. Sameen and B. Pradhan, "Landslide detection using residual networks and the fusion of spectral and topographic information," *IEEE Access*, vol. 7, pp. 114363–114373, 2019. [Online]. Available: https://www.semanticscholar.org/paper/7d0c946386b99e9782d1e3e966ebcaaf5574b4cc

[21] C. Ye et al., "Landslide detection of hyperspectral remote sensing data based on deep learning with constrains," *IEEE J. Sel. Topics Appl. Earth Observ. Remote Sens.*, vol. 12, no. 12, pp. 5047–5060, Dec. 2019. [Online]. Available: https://ieeexplore.ieee.org/document/8911205/

[22] W. Wiratama and D. Sim, "Fusion network for change detection of high-resolution panchromatic imagery," *Appl. Sci.*, vol. 9, no. 7, Apr. 2019, Art. no. 1441. [Online]. Available: https://www.mdpi.com/2076-3417/9/7/1441

[23] H. Zhao, F. Liu, H. Zhang, and Z. Liang, "Convolutional neural network based heterogeneous transfer learning for remote-sensing scene classification," *Int. J. Remote Sens.*, vol. 40, no. 22, pp. 8506–8527, Nov. 2019. [Online]. Available: https://www.tandfonline.com/doi/full/10.1080/01431161.2019.1615652

[24] C. Tang, C. J. Van Westen, H. Tanyas, and V. G. Jetten, "Analysing post-earthquake landslide activity using multi-temporal landslide inventories near the epicentral area of the 2008 Wenchuan earthquake," *Natural Hazard Earth Syst. Sci.*, vol. 16, no. 12, pp. 2641–2655, Dec. 2016. [Online]. Available: https://nhess.copernicus.org/articles/16/2641/2016/

[25] M. Tang et al., "Activity law and hydraulics mechanism of landslides with different sliding surface and permeability in the three Gorges Reservoir Area, China," *Eng. Geol.*, vol. 260, Oct. 2019, Art. no. 105212. [Online]. Available: https://linkinghub.elsevier.com/retrieve/pii/S0013795218304538

[26] C. Zhang et al., "A deeply supervised image fusion network for change detection in high resolution bi-temporal remote sensing images," *ISPRS J. Photogrammetry Remote Sens.*, vol. 166, pp. 183–200, Aug. 2020. [Online]. Available: https://linkinghub.elsevier.com/retrieve/pii/S0924271620301532

[27] H. Wang, Q. Guo, X. Ge, and L. Tong, "A spatio-temporal monitoring method based on multi-source remote sensing data applied to the case of the Temi landslide," *Land*, vol. 11, no. 8, Aug. 2022, Art. no. 1367. [Online]. Available: https://www.mdpi.com/2073-445X/11/8/1367

[28] Q. Guo, L. Tong, and H. Wang, "A monitoring method based on vegetation abnormal information applied to the case of Jizong shed-tunnel landslide," *Remote Sens.*, vol. 14, no. 22, Nov. 2022, Art. no. 5640. [Online]. Available: https://www.mdpi.com/2072-4292/14/22/5640

[29] J. Wang, W. Li, Y. Wang, R. Tao, and Q. Du, "Representation-enhanced status replay network for multisource remote-sensing image classification," *IEEE Trans. Neural Netw. Learn. Syst.*, pp. 1–13, 2023.

[30] M. Zhang, W. Li, X. Zhao, H. Liu, R. Tao, and Q. Du, "Morphological transformation and spatial-logical aggregation for tree species classification using hyperspectral imagery," *IEEE Trans. Geosci. Remote Sens.*, vol. 61, pp. 1–12, Jan. 2023, Art. no. 5501212. [Online]. Available: https://ieeexplore.ieee.org/document/10005092/

[31] C. Zhang, W. Jiang, Y. Zhang, W. Wang, Q. Zhao, and C. Wang, "Transformer and CNN hybrid deep neural network for semantic segmentation of very-high-resolution remote sensing imagery," *IEEE Trans. Geosci. Remote Sens.*, vol. 60, pp. 1–20, Jan. 2022, Art. no. 4408820. [Online]. Available: https://ieeexplore.ieee.org/document/9686732/

[32] S. A. Kamran, K. F. Hossain, A. Tavakkoli, S. A. Baker, and S. L. Zuckerbrod, "SwinVFTR: A novel volumetric feature-learning transformer for 3D OCT fluid segmentation," 2023, *arXiv:2303.09233*.

[33] M. Van Nguyen, V. D. Lai, A. P. B. Veysh, and T. H. Nguyen, "Trankit: A light-weight transformer-based toolkit for multilingual natural language processing," in *Proc. 16th Conf. Eur. Chapter Assoc. Comput. Linguistics: Syst. Demonstrations*, 2021, pp. 80–90.

[34] J. M. J. Valanarasu, P. Oza, I. Hacihaliloglu, and V. M. Patel, "Medical transformer: Gated axial-attention for medical image segmentation," in *Proc. Int. Conf. Medical Image Comput. Comput.-Assisted Intervention*, 2021, pp. 36–46.

[35] H. Zhao, L. Jiang, J. Jia, P. H. S. Torr, and V. Koltun, "Point transformer," in *Proc. IEEE/CVF Int. Conf. Comput. Vis.*, 2021, pp. 16239–16248.

[36] Y. Huang et al., "How spatial resolution of remote sensing image affects earthquake triggered landslide detection: An example from 2022 Luding earthquake, Sichuan, China," *Land*, vol. 12, no. 3, Mar. 2023, Art. no. 681. [Online]. Available: https://www.mdpi.com/2073-445X/12/3/681

[37] A. Vaswani et al., "Attention is all you need," in *Proc. 31st Int. Conf. Neural Inf. Process. Syst.*, 2017, pp. 6000–6010.

[38] Z. Liu et al., "Swin transformer: Hierarchical vision transformer using shifted windows," in *Proc. IEEE/CVF Int. Conf. Comput. Vis.* 2021, pp. 9992–10002. [Online]. Available: https://ieeexplore.ieee.org/document/9710580/

[39] A. álvarez and T. Ritchey, "Applications of general morphological analysis," *Acta Morphologica Generalis*, vol. 4, no. 1, pp. 1–40, 2015.

[40] F. Wang, E. Wu, S. Chen, and H. Wu, "Texture feature extraction and morphological analysis of landslide based on image edge detection," *Math. Problems Eng.*, vol. 2022, pp. 1–12, Jul. 2022. [Online]. Available: https://www.hindawi.com/journals/mpe/2022/2302271/

[41] T. W. Yeh and R. Y. Chuang, "Morphological analysis of landslides in extreme topography by UAS-SfM: Data acquisition, 3D models and change detection," *Int. Arch. Photogrammetry, Remote Sens., Spatial Inf. Sci.*, vol. 43, pp. 173–178, Aug. 2020. [Online]. Available: https://isprs-archives.copernicus.org/articles/XLIII-B5-2020/173/2020/

[42] B. Cheng, R. Girshick, P. Dollar, A. C. Berg, and A. Kirillov, "Boundary IoU: Improving object-centric image segmentation evaluation," in *Proc. IEEE/CVF Conf. Comput. Vis. Pattern Recognit.*, 2021, pp. 15329–15337. [Online]. Available: https://ieeexplore.ieee.org/document/9578118/

Jianqiang Zhang received the Ph.D. degree in the distribution and risk assessment of landslides triggered by the Wenchuan earthquake from the Institute of Mountain Hazards and Environment, Chinese Academy of Sciences, Chengdu, China, in 2011.

He is currently an Associate Professor with the Institute of Mountain Hazards and Environment, Chinese Academy of Sciences, and also with the Key Laboratory of Mountain Hazards and Earth Surface Process, Institute of Mountain Hazards and Environment, Chinese Academy of Sciences. He has long been committed to the research of remote sensing identification and susceptibility assessment and risk assessment of mountain disasters, such as landslides and debris flows. His research interests include comprehensive risk assessment and risk change of mountain disasters.

Haiqing He received the Ph.D. degree in geodesy and survey engineering from Wuhan University, Wuhan, China, in 2013.

He is currently a Full Professor with the School of Surveying and Geoinformation Engineering, East China University of Technology, Nanchang, China, and also with the Key Laboratory of Mine Environmental Monitoring and Improving around Poyang Lake of Ministry of Natural Resources, East China University of Technology. His research interests include photogrammetry and remote sensing, image processing, and machine learning.

Yang Jia, photograph and biography not available at the time of publication.

Rong Chen, photograph and biography not available at the time of publication.

Yonggang Ge, photograph and biography not available at the time of publication.

Zaiyang Ming, photograph and biography not available at the time of publication.

Lili Zhang, photograph and biography not available at the time of publication.

Haoyu Li, photograph and biography not available at the time of publication.

Yu Huang is currently working toward the M.Sc. degree in remote sensing and mountain hazard detection with the School of Surveying and Geoinformation Engineering, East China University of Technology, Nanchang, China, and the Institute of Mountain Hazards and Environment, Chinese Academy of Sciences, Chengdu, China.

His research interests include drone and satellite image processing and machine learning for natural disaster management.